European Polymer Journal 180 (2022) 111575

Contents lists available at ScienceDirect

European Polymer Journal

journal homepage: www.elsevier.com/locate/europolj

Functional aerogel coatings on tetrakaidecahedron lattice

Piljae Joo [1], Aparna Agrawal [1], Yimin Yao, Nicholas Teo, Sadhan C. Jana *

School of Polymer Science and Polymer Engineering, The University of Akron, Akron, OH 44325, The United States

ARTICLE INFO

Keywords:
Polyimide
Aerogel skin
Additive manufacturing
Stereolithography
Metamaterials
Kelvin cell
Tetrakaidecahedron lattice

ABSTRACT

This paper reports a new method of functional metamaterial structure fabrication based on ultra-porous aerogel skins introduced on the surfaces of solid tetrakaidecahedron lattices obtained via 3D-printing tools. The solid tetrakaidecahedron lattice shapes are first fabricated from acrylate resin systems using a stereolithography printer. The lattice is then coated with a skin of polyimide gel via sol–gel reaction process, post-curing, and solvent-aging. The aerogel skin is recovered from the gel using supercritical drying. The lattice is found uniformly coated with polyimide aerogel skin as confirmed from examination of surface morphology via scanning electron microscopy and X-ray tomography imaging. The concept is extended to coatings by silica and Kevlar aerogel systems. The mechanical and thermal properties of the resultant materials and a set of applications are discussed.

1. Introduction

The unique structural organizations render conventional materials into shapes with architectural and aesthetical attributes often with unusual properties [1]. In this context, the current focus on metamaterials research is timely. Metamaterials do not exist in nature and must be architecturally synthesized to derive many extraordinary physical properties from their unique geometrical shapes, instead of more conventional approach based on material compositions [2,3]. The desired unique properties are often achieved via patterning certain shapes at a controlled length scale using photolithography, [4] electron-beam lithography, [5] ion-beam lithography [6], and nanoimprint lithography [7]. In the past decade, metamaterials research primarily focused on mechanical metamaterials buoyed by the success of additive manufacturing technologies enabling the fabrication of unconstrained architectures derived often from imaginary designs [3].

Re-entrant [8–10] and hexagonal [11,12] lattice structures are popularly studied because of their exceptional acoustic absorption and strong mechanical properties via control of the Poisson's ratio. Traditionally used manufacturing techniques such as micromachining often suffer from the loss of precision in fabrication of lattice structures [10]. However, the advent of additive manufacturing enables fabrication of 3D lattice structures with the strut-and-node arrangements that help realize the full intrinsic properties of lattice structures. Models with complex architectures are now tangible, courtesy to the innovative additive manufacturing tools [3].

A category of metamaterials with outstanding synergetic performance can be manufactured by rendering functional material coatings onto 3D-printed solid metamaterial architectures. Schaedler et al. [13] introduced a method of solid metal-electroless nickel plating on to 3D sacrificial template and observed unique mechanical functions from the resultant metamaterial structures such as complete shape recovery after compression at high strains, high energy absorption capability, and a quadratic scaling relationship between Young's modulus (E) and density (ρ), $E \sim \rho^2$. Gao et al. [14] produced metal-sputtered mechanical metamaterials with enhanced mechanical properties such as higher specific strength and ductility under compressive loading. These studies served as a motivation for the present work whereby metamaterials were manufactured with aerogel skin layers.

Polymer-based aerogels have been successfully used in various applications that extend the promise laid out by fragile silica aerogels. [15–17] Polymer-based aerogel media with mostly fibril-like networks find applications in air filtration and liquid–liquid separation. Kim et al. [18–20] elaborated high efficiency airborne nanoparticle filtration with no compromise on air permeability using syndiotactic polystyrene (sPS) aerogels [18], a hybrid of sPS-polyvinylidene fluoride aerogels [19], and a hybrid of sPS-silica aerogels [20]. These authors established a direct correlation between nanoparticle filtration efficiency and the mesopore content of the aerogel and reported that static surface charge significantly improves filtration performance. Wang et al. [21] demonstrated

* Corresponding author.
E-mail address: janas@uakron.edu (S.C. Jana).
[1] These authors contributed equally to this work.

https://doi.org/10.1016/j.eurpolymj.2022.111575
Received 30 June 2022; Received in revised form 5 September 2022; Accepted 7 September 2022
Available online 24 September 2022

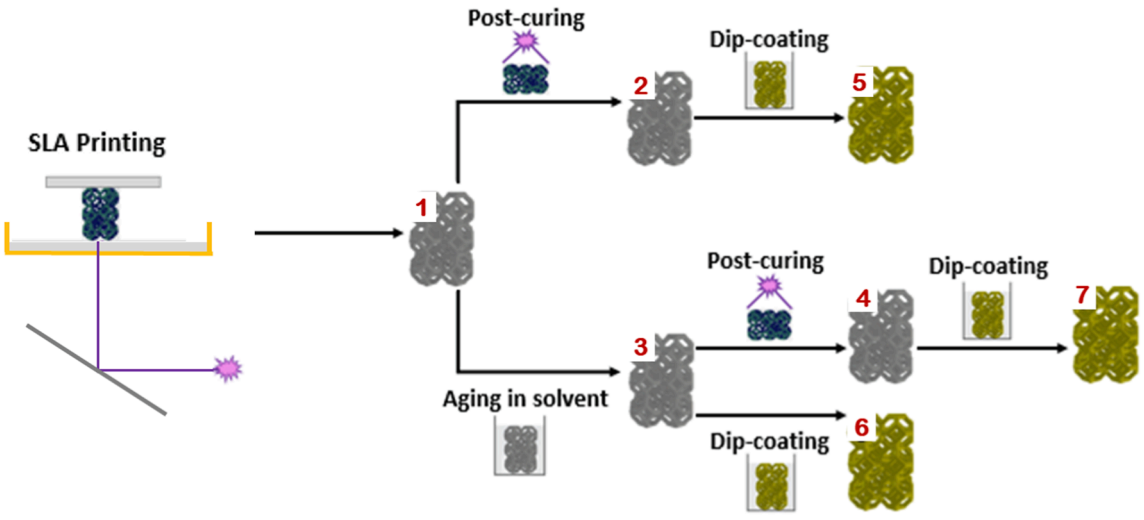

Fig. 1. Schematic showing printing of the tetrakaidekahedral lattice (shown as 1) and procedure of post-curing under 405 nm wavelength light (2 and 4), aging in DMF solvent (3), and dip-coating (5,6, and 7), all conducted at room temperature.

fast and efficient oil–water separation using polyimide aerogel under harsh conditions. Zhai and Jana [22] produced a series of polyimide aerogel filter media and reported that macropore and mesopore contents are responsible respectively for air permeability and airborne nanoparticle filtration efficiency. Ghaffari et al. also reported the role of bimodal macro and mesoporous structures of polyimide aerogel on air permeability [23].

In this work, a fabrication strategy was investigated to combine the attributes of high porosity polyimide aerogels with mechanical metamaterials in the form of 3D-printed tetrakaidekahedral polyacrylate resin lattice structures. The concept was then extended to two additional aerogels - silica and Kevlar – for demonstrating the adaptability of the process to suit different aerogel chemistries. We earlier reported a facile method of fabrication of complex-shaped polyimide aerogel structures by using sacrificial gyroid shape mold manufactured using fused filament fabrication method [24]. Agrawal et al. [25] reported fabrication of polyurethane aerogels in re-entrant honeycomb forms to achieve auxeticity and much higher flexibility compared to corresponding aerogel monoliths. Our group also demonstrated fabrication of fully scalable modular aerogel bricks that offered excellent thermal insulation and high mechanical strength [26].

It is acknowledged that most metamaterials reported in literature are fabricated from acrylate resins using stereolithography (SLA) technique to obtain higher resolution than possible with fused filament fabrication. [27,28] In the present study, a high-resolution SLA technique was used to fabricate a polyacrylate metamaterial structure. The skins of aerogels were developed on the metamaterial surfaces using a sol–gel process. The aerogel skins of polyimide, silica, and Kevlar were separately developed to demonstrate the utility of the fabrication process to three different sol–gel chemistry systems. Such materials may be used in a number of applications, such as in liquid removal, airborne nanoparticle filtration, or fast vapor absorption.

The growth of aerogel skins on metamaterial structures is not obvious. In this work, the surface of the polyacrylate tetrakaidekahedral structure was tuned by solvent-aging and post-curing to obtain desired crosslink density appropriate for diffusion of precursor sol materials. Although the curing and aging process did not significantly affect the quality of aerogel coating, the color and the mechanical properties of the samples significantly changed due to the cracks induced by the solvent-aging step. The surface polarity, thermal properties, and compressive mechanical properties were evaluated. The open-cell tetrakaidekahedral lattice offers low packaging size [29,30] involving large flow channels indicating that the aerogel-coated tetrakaidekahedral lattices may be used as an architecture-controlled 3D filter component.

2. Experimental

2.1. Materials

Pyromellitic dianhydride (97 %, M_w ~ 218 g/mol) (PMDA) was purchased from Alfa-Aesar (Haverhill, MA), 2,2′-dimethylbenzidine (M_w ~ 212 g/mol) (DMBZ) was purchased from Shanghai Worldyang Chemical Cp. ltd (Shanghai, China), tris(2-aminoethyl)amine (97 %, M_w ~ 230 g/mol) (TREN) crosslinker, nitric acid (65–67 %, M_w ~ 63 g/mol), and ammonium hydroxide solution (28–30 % NH_3 basis, M_w ~ 35 g/mol) were obtained from Sigma Aldrich (Milwaukee, WI). Pyridine (≥ 99 %, M_w ~ 79 g/mol), acetic anhydride (≥ 99 %, M_w ~ 102 g/mol), ethanol, and acetone were purchased from Fisher Scientific (Ontario, NY). For the synthesis of silica aerogel, the reactant tetraethyl orthosilicate (reagent grade, 98 %, M_w ~ 208 g/mol) (TEOS) was purchased from Scientific Polymer Products Inc. (Ontario, NY). In order to prepare Kevlar aerogel, Kevlar fibers (Size 69) were purchased from The Thread Exchange, Inc. (Weaverville, NC). N,*N*-dimethylformamide (DMF) and dimethyl sulfoxide (DMSO) were purchased from VWR International (Radnor, PA). A high-temperature SLA acrylate resin was purchased from Formlabs (Somerville, MA). For contact anle measurement, methylene iodide was purchased from Sigma Aldrich.

2.2. Preparation of the lattices

The tetrakaidekahedral lattice template was designed in Solidworks® and printed via SLA using a Form2 printer from Formlabs (Somerville, MA). The thickness of each layer was set up to 50 μm and 3.6 mL of resin was consumed for printing of one tetrakaidekahedral lattice.

2.3. Post-processing and polyimide (PI) coating on the lattices

Previous studies reported that polyimide gels are traditionally prepared by a reaction of dianhydrides and diamines (e.g., PMDA and DMBZ) with a trifunctional amine (e.g., TREN) acting as a crosslinker followed by a chemical imidization step. Polyimide aerogels are then obtained through supercritical drying of these gels [15,31,32]. Here, the SLA printed lattices were subjected to different post-processing steps, such as curing by 405 nm light exposure for 20 min, aging in DMF solvent for 24 h, or both processes, all conducted at room temperature. The

resultant lattice materials were immersed in 80 mL of DMF solution containing 6.3 g of PMDA for 24 hrs. Next, 6.3 g DMBZ dissolved in 40 mL of DMF was added into the solution to form polyamic acid oligomers in the presence of immersed lattice materials. Subsequently, 1.2 g TREN in 30 mL of DMF and 19.95 g acetic anhydride and 18.75 g pyridine were added to the polyamic acid solution to obtain crosslinked and imidized network of polyimide gel [31]. The target concentration of solid in the polyimide sol was 6.7 wt%, and all chemical reactions were carried out under magnetic stirring at room temperature. The sol–gel transition takes 15 mins at this solid concentration. This value is similar to the value reported by Teo et al. for polyimide aerogels of similar formulations [31]. However, the sol was allowed to stand for 12 h at room temperature to ensure that a fully crosslinked network of polyimide coating on polyacrylate lattices was formed. The coated lattices were subjected to solvent-exchange in solvent mixtures of 100 % DMF, 75 % DMF/25 % acetone, 50 % DMF/50 % acetone, 25 % DMF/75 % acetone, and finally 100 % acetone each at 12-hour intervals. The loosely held polyimide gel chunks were removed by dragging the structures in the liquid during the first solvent exchange step in 100 % DMF. The lattice specimens with and without polyimide gel coating were transferred into an autoclave, washed with liquid carbon dioxide, and dried under the supercritical condition of carbon dioxide at 50 °C and 11 MPa to obtain dried specimens. The entire process illustrating the production of specimens is schematically shown in Fig. 1 and **Figure S1**. The final specimens obtained in steps 5,6, and 7 in Fig. 1 were used in characterization.

2.4. Silica coating on the lattice

The polyacrylate lattice specimens were also coated with silica aerogel to demonstrate the adaptability of the process for rendering inorganic oxide coatings onto the lattice. Silica aerogels are well-known for their fire retardance [33] and thus a silica aerogel coating can impart fire retardance to the polyacrylate lattices. Printed polyacrylate lattice specimens were swollen in DMF for 24 h and then the solvent was exchanged with ethanol for 2 days. The specimens were transferred to a mixture of 41.6 g of TEOS, 10.8 mL deionized (DI) water, and 80 mL ethanol. After 24 h, nitric acid was added until pH of the solution reached a value of 2.0. For gelation, a mixture of 1 mL ammonium hydroxide, 14.4 mL DI water, and 60 mL ethanol was added. The loosely held silica gel was removed during the first stage of the solvent exchange step in ethanol. Eventually, the solvent was entirely exchanged with 100 % ethanol and the silica-coated lattice was dried under supercritical condition of carbon dioxide.

2.5. Aramid coating on the lattice

For coating the printed polyacrylate specimens with an aramid aerogel, poly (p-phenylenediamine terephthalamide) also known as Kevlar was used. Kevlar is a high-performance material and Kevlar aerogels have very high porosity (~99 %) and permeability providing advantages for adsorption applications. The procedure for coating the SLA printed specimen with Kevlar aerogel is outlined below. First, a dispersion of Kevlar was produced by magnetically stirring 1 % by weight of Kevlar fibers in 100 mL DMSO in the presence of 1 g KOH for 1 week. Next, the polyacrylate lattices were printed via SLA and swollen in DMF and solvent exchanged with ethanol in a similar way as described for silica gel coating. The resultant polyacrylate lattice was then transferred to a container holding 60 mL of the Kevlar dispersion and the system was magnetically stirred for 2 days which introduced a layer of Kevlar dispersion onto the polyacrylate lattice. The lattice specimen was transferred to deionized water (DI water) which caused gelation of the Kevlar layer. The specimens were solvent exchanged with DI water every 2 h for 5 times to remove any excess of DMSO followed by solvent exchanges with ethanol every 2 h for 5 times. The specimens were supercritically dried using carbon dioxide.

2.6. Characterization

Compression test: The stress vs strain behavior of the lattices was obtained using an Instron 5567 tensiometer (Norwood, MA). For this, a 100 N load cell was used with a compression rate of 1.3 mm/min.

Morphology: The morphology of the lattices was captured using a LYRA3 scanning electron microscope (SEM, Tescan, CZ) at an accelerating voltage of 5 kV. A representative piece of each fractured lattice strut was placed on an aluminum stub using carbon tape, followed by sputter coating with silver (ISI-5400 Sputter Coater, Polaron, UK). An optical microscope (BX51, Olyumpus, JP) was used to observe the polyimide aerogel layer on the lattices.

Thermogravimetric analysis (TGA): TGA was conducted under nitrogen atmosphere with a Q50 thermogravimetric analyzer (TA Instruments, Waltham, MA) using a heating rate of 10 °C/min up to 700 °C under N_2 atmosphere at a flow rate of 40 mL/min.

Infra-red (IR) spectroscopy: IR spectra was obtained by Alpha-P FT-IR spectroscope (Brucker, Billerica, MA). The FTIR spectrum was obtained to analyze the change in chemical composition of all the specimens involved. First, 128 scans of background were taken to get the baseline followed by 128 scans of the samples. The samples were scanned with a resolution of 4 cm^{-1}.

Skeletal density: The values of skeletal density were obtained using a helium pycnometer (AccuPyc II 1340, Micromeritics Instrument Corp., Norcross, GA). The pycnometer chamber was calibrated and flushed with helium 25 times before use and the measurements were performed at room temperature.

X-ray micro-computed tomography (μCT): The cross-sectional images of the struts from the tetrakaidekahedral lattices were taken by SkyScan 1172 X-ray μCT (Brucker, Billerica, MA) at a source voltage of 32–33 kV and a source current of 193–198 μA.

Contact angle (CA) measurement: The CA values of deionized water and methylene iodide on representative polymer surfaces were collected using a Ramé-Hart (Succasunna, NJ) Model 500 standard contact angle goniometer. The values of polymer surface free energy and polarity were calculated based on Wu's theory [34] as presented in Eqs. (1)–(3).

$$\gamma_{12} = \gamma_1 + \gamma_2 - \frac{4\gamma_1^d\gamma_2^d}{\gamma_1^d + \gamma_2^d} - \frac{4\gamma_1^p\gamma_2^p}{\gamma_1^p + \gamma_2^p} \tag{1}$$

Eq. (1) can be rearranged to the form given in equation (2) for facilitating calculation of surface energy values.

$$(b_i + c_i - a_i)\gamma^d\gamma^p + c_i(b_i - a_i)\gamma^d + b_i(c_i - a_i)\gamma^p - a_i b_i c_i = 0 \tag{2}$$

Eqs. (1) and (2), γ^d and γ^p are the dispersion and polar components respectively of surface energy (γ_{12}) of the polymer; $a_i = \left(\frac{\gamma_i(1+cos\theta_i)}{4}\right), b_i = \gamma_i^d, c_i = \gamma_i^p$; θ_i is contact angle of water or methylene iodide on the polymer. The values of surface energy of water$\gamma_1 = 72.8$ dynes/cm with $\gamma_1^d = 22.1$ dynes/cm and $\gamma_1^p = 50.7$ dynes/cm and surface energy of methylene iodide$\gamma_2 = 50.8$ dynes/cm with $\gamma_2^d = 44.1$ dynes/cm and $\gamma_2^p = 6.7$ dynes/cm were used in surface energy calculation [34]. The surface polarity was calculated as in Eq. (3),

$$\text{Polarity} = \frac{\gamma^p}{\gamma^p + \gamma^d} \tag{3}$$

3. Results and discussion

At the outset, we focused on the integrity of PI gel coating on polyacrylate lattice surfaces. As a first approximation, the polarity values of PI and polyacrylate lattice structures right after 3D printing and post-curing processes were determined from the values of contact angle of water and methylene iodide on 3D-printed sheets of polyacrylate and compressed sheets of PI aerogel. The PI aerogel specimens were compressed at 1200 psi pressure to remove the pores so that only the surface

Table 1
Surface free energy and polarity from contact angle values of as printed and post-cured polyacrylate sheet and compressed polyimide aerogel sheet.

Material	Contact angle (°)		Surface free energy (dynes/cm)			Polarity
	Water	Methylene iodide	γ^d	γ^p	γ	γ^p/γ
As printed sheet	97 ± 2	58 ± 2	27.4	4	31.4	0.13
Post-cured sheet	106 ± 2	67 ± 2	27.4	0.9	28.4	0.03
Compressed PI aerogel sheet	82 ± 2	36 ± 1	33.7	8.8	42.5	0.21

energy values due to chemical composition could be captured. The polar component of the surface energy and the polarity values are listed in Table 1. It is evident from the data that the polarity of PI gel (0.21) was much closer to the as printed polyacrylate sheet specimen (0.13) than the ones produced by post-curing (0.03). One may extend this observation to achieving stronger adhesion of PI aerogel coating on the as printed specimen than the post-cured one. We also obtained contact angle values of droplets of DMF on the polyacrylate surface to understand the wetting characteristics of printed acrylate specimens by DMF, the solvent used in preparation of PI gel. We note that the formation of a uniform coating by PI gel on acrylate surface is contingent upon excellent wetting of the surface by DMF. The values of contact angle of DMF droplets on the surface of as printed and post-cured acrylate specimens were 18.23° and 16.3° respectively. These values indicate good wetting characteristics of polyacrylate surfaces by DMF.

The dip-coating behavior of the polyacrylate lattices in PI sol was investigated next. As presented in Experimental section, the tetrakaidekahedral lattice specimens were printed from the acrylate-based resin by the SLA method. Sequentially, different post-processing steps were executed. Different specimens evaluated henceforth are designated as follows - Sample #1 represents the as printed acrylate specimen, Sample #2 the acrylate specimen post-cured at 405 nm wavelength, Sample #3 represents the acrylate specimen swelled in DMF, Sample #4 is the specimens first swelled in DMF followed by post-curing at 405 nm wavelength, Sample #5 represents the post-cured acrylate (Sample #2) coated with PI, Sample #6 is PI-coated Sample #3, and Sample #7 is Sample #4 coated with PI. The specimen designations are summarized in Fig. 2.

It is seen in **Figure S2** that the post-curing process induced yellow color in Sample #2 in comparison to the as printed Sample #1. Sample #3 was swollen in DMF for 24 h and no change in color was seen in this case. The post-curing process induced some yellowness also in Sample #4. One can infer that the specimen dimensions of images 3 and 4 changed due to swelling in DMF as in **Figure S2**. The length and height of the lattice and the thickness of the strut in the lattice changed due to swelling as follows – length increased by 9.1 % (24.25 mm to 26.45 mm), height increased by 9.4 % (36.06 mm to 39.47 mm), and strut thickness increased by 17 % (2.05 mm to 2.4 mm). Sample # 4, which was a post-cured sample of #3, became more yellowish than #3. The post-curing induced a higher chroma of the sample color (**Figure S2**).

It is noted that the dimensions of Samples #3 and #4 after solvent exchange with acetone and drying under super-critical condition returned close to the dimensions of as-printed acrylate specimens (Sample #1 and #2), see Fig. 2. Interestingly, the solvent-aged samples display deeper yellow than the unaged Sample #5, and the additionally post-cured Sample #7 shows the deepest yellow color compared to Sample #6. Thus, it can be inferred that the post-curing process tends to change the color of specimens and the aging step in the solvent led to volume expansion, which in turn made way for PI precursor molecules to enter the swollen acrylate domains, thus producing even deeper yellow color, as shown in Fig. 2.

The supercritically dried specimens that were earlier subjected to aging in DMF, e.g., Sample #3 and Sample #4, showed considerable cracks in the lattice structures. However, the PI gel coated specimens Sample #6 and Sample #7 showed much less damage than Sample #3 and Sample #4. Sample #5 was not visibly damaged. The DMF molecules easily penetrated the less crosslinked polyacrylate network leading to expansion of the volume of the network. To capture these trends, we

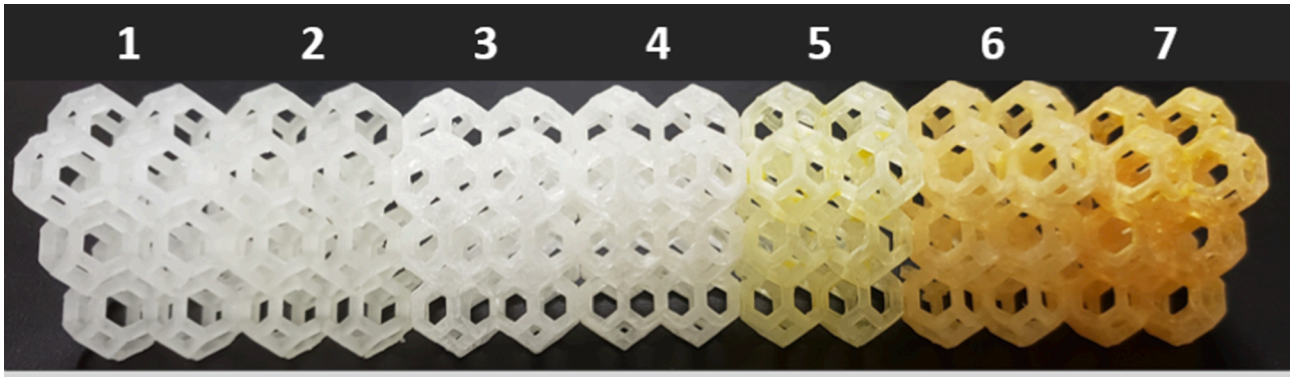

	Post-curing	Aging in solvent	Post-curing after aging in solvent	PI-Coating
#1. As printed lattice	X	X	X	X
#2. Post-cured lattice	O	X	X	X
#3. Expanded lattice	X	O	X	X
#4. Expanded_cured lattice	X	O	O	X
#5. Post-cured_PI-coated lattice	O	O	X	O
#6. Expanded_PI-coated lattice	X	O	X	O
#7. Expanded_cured_PI-coated lattice	X	O	O	O

Fig. 2. The color and appearance of tetrakaidekahedral lattices as function of different post-curing and solvent aging steps.

Table 2
Skeletal density of post-processed tetrakaidekahedral lattices.

Sample	Skeletal density (g/cm^3)
#0. PI aerogel monolith	1.3697
#1. As printed lattice	1.2053
#2. Post-cured lattice	1.2156
#3. Expanded lattice	1.2118
#4. Expanded-cured lattice	1.2111
#5. Post-cured_PI coated lattice	1.2149
#6. Expanded_PI coated lattice	1.2126
#7. Expanded_cured_PI coated lattice	1.2153

prepared cylindrical specimens of 1 cm diameter from each material and subjected them to the same post-processing step as shown in Fig. 2. A set of representative images are shown in **Figure S3.** It is evident that Sample #5 did not have macroscopic damage and that PI-coated specimens Sample #6 and Sample #7 showed less cracks than Sample #3 and Sample #4.

The skeletal density of supercritically dried specimens was measured to verify any weight loss due to aging in solvent or to obtain the amount of polyimide coating on the tetrakaidekahedral lattices (see Table 2). As reference, the skeletal density values of PI aerogel and as printed polyacrylate specimens were respectively 1.3697 g/cm^3 and 1.2052 g/cm^3. It is evident that post-curing and solvent aging rendered acrylates a bit denser with skeletal density varying from 1.2156 g/cm^3 for post-cured

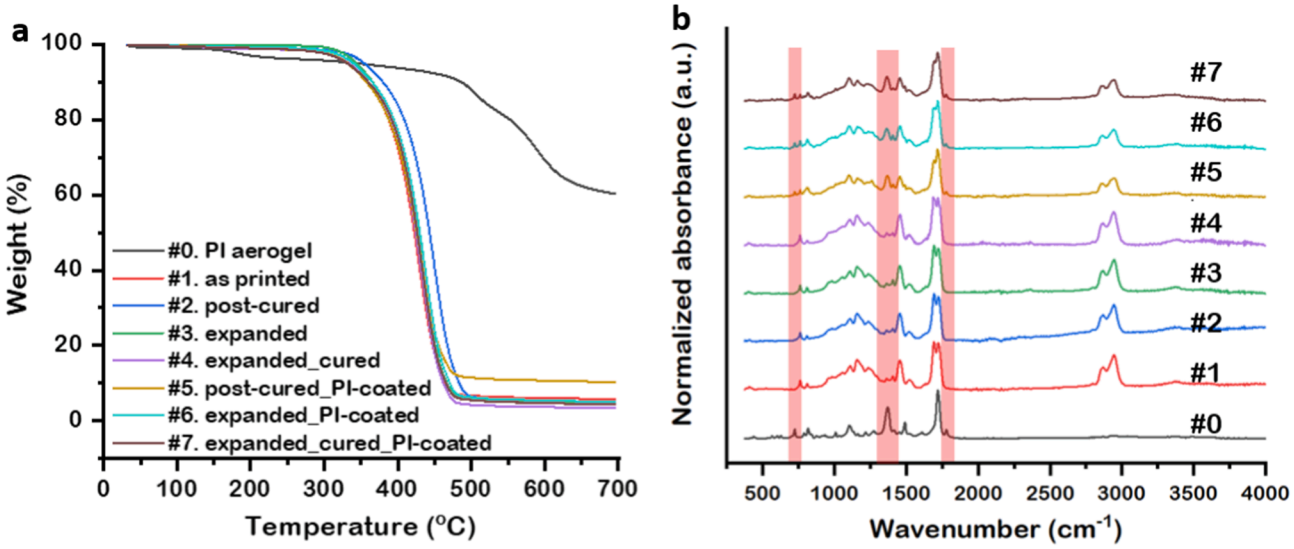

Fig. 3. (a) TGA traces and (b) FT-IR spectra of different post-processed tetrakaidekahedral lattices. Sample #0 refers to PI aerogel.

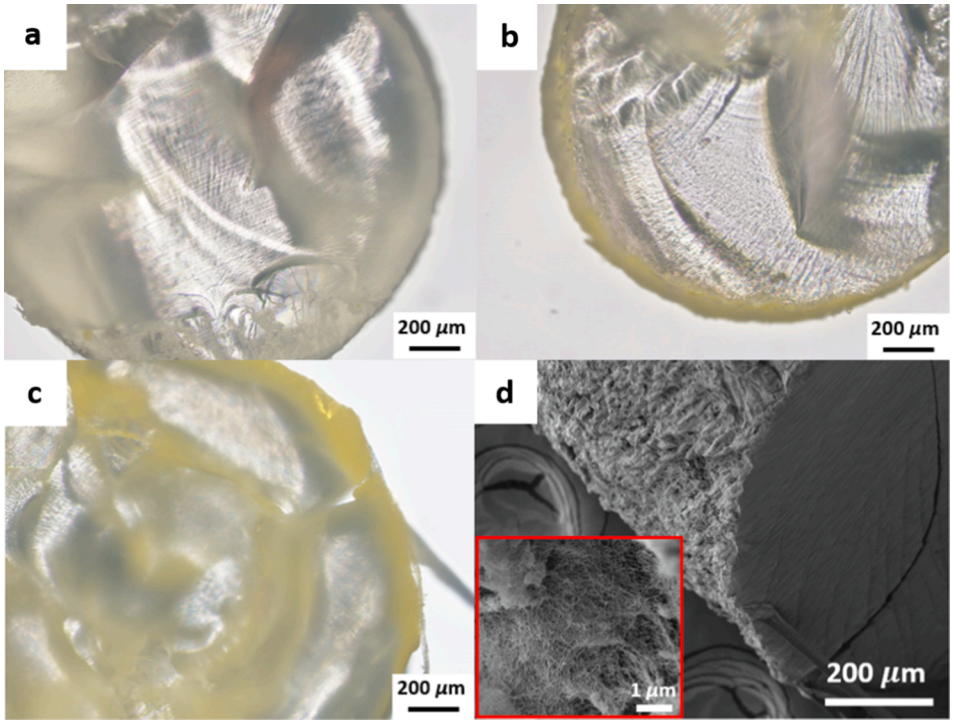

Fig. 4. Optical microscope images from cross-sectional fragment of (a) #2 post-cured lattice, (b) #5 post-cured PI-coated lattice and (c) #6 expanded, PI-coated lattice, and (d) SEM image of #6 expanded, PI-coated lattice.

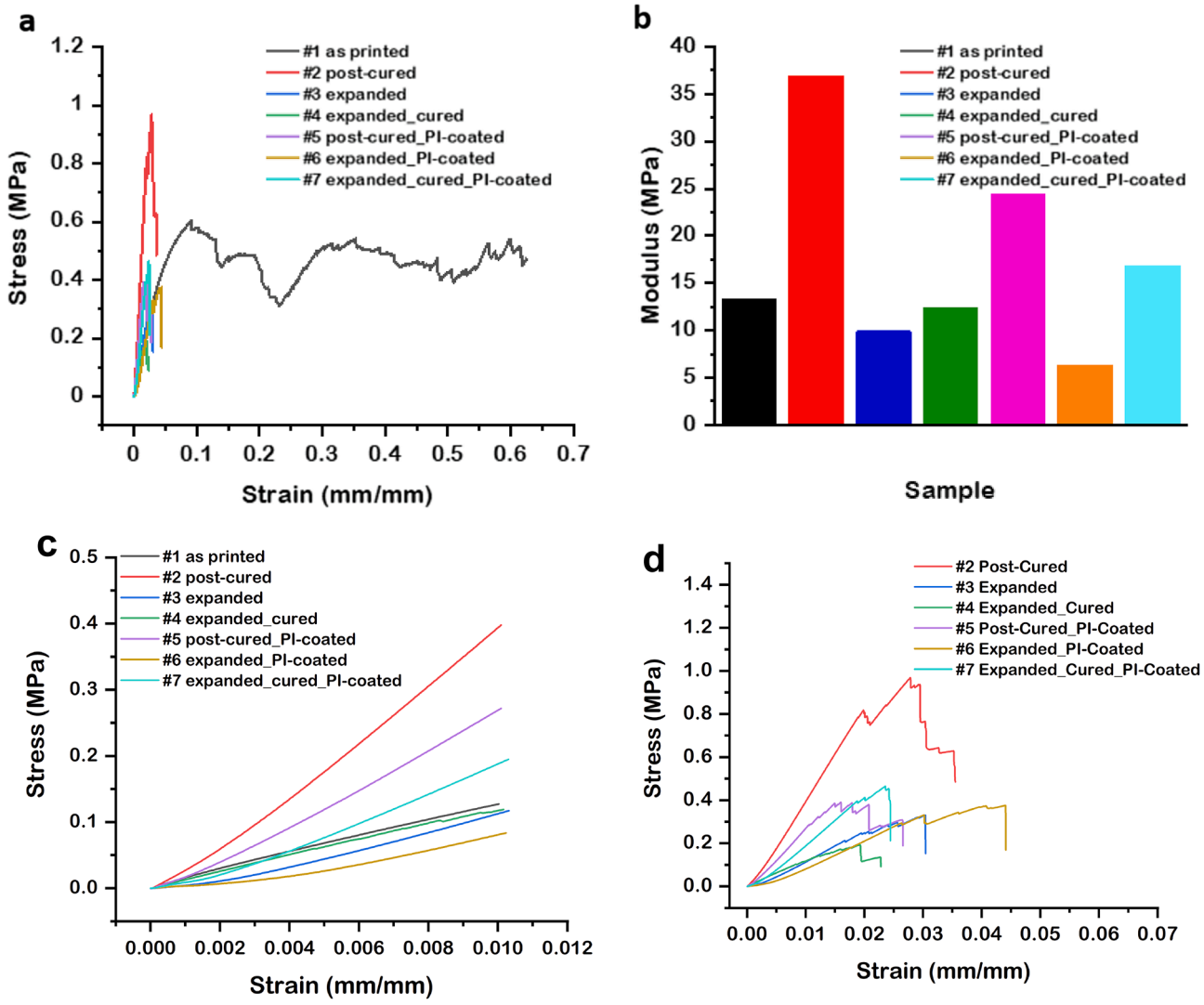

Fig. 5. (a) Compressive stress vs strain curves, (b) compressive modulus and (c) compressive stress vs strain curves at low strain (d) compressive stress vs strain curves under 0.1 strain.

lattice (Sample #2) to 1.2118 g/cm^3 for solvent-aged lattice (Sample #3) to 1.2111 g/cm^3 for solvent-aged and post-cured (Sample #4) specimens. The skeletal density of PI-aerogel coated specimens (Sample #5, #6, and #7) fell in the same range as post-cured and solvent-aged polyacrylate lattices, e.g., 1.2149 g/cm^3 for Sample #5, 1.2126 g/cm^3 for Sample #6, and 1.2153 g/cm^3 for Sample #7. Considering the above skeletal density values, we contend that the amount of PI aerogel coating on the lattices was significantly small.

In view of low thermal conductivity of PI aerogel, typically around 30 mW (m K)$^{-1}$ [35,36] and high thermal stability up to 525 °C [31] we performed TGA measurements to identity the role of PI aerogel coating at slow temperature increments. Such data are presented in Fig. 3(a). It is seen that all polyacrylate lattices showed similar decomposition trend and lost 10 % of weight at 360 °C, except the post-cured Sample #2 that lost 10 % weight at 373 °C. Note that PI aerogel lost 10 % weight at 485 °C. PI aerogel-coated Sample #5 sample lost 10 % weight at 360 °C, about 13 °C earlier than Sample #2. This is attributed to macroscopic damages in the specimens due to exposure of DMF during the PI-coating process.

The FT-IR spectra in Fig. 3(b) show matching peaks for Sample #0 (PI aerogel) and Sample #5–7. The presence of distinguishable peaks at 728, 1366, and 1777 cm^{-1} indicate the presence of imide groups from PI aerogel coating. Sample #1 and #2 exhibit almost the same peak ratio and the positions although they had different crosslink density.

Further, the formation of PI aerogel coating on acrylate rods and struts was monitored using optical microscope and SEM images. Fig. 4 **(b)** corresponding to Sample #5 clearly shows the distinctive yellow border near the edges due to PI aerogel compared to Fig. 4 **(a)** for Sample #2. More interestingly, Fig. 4 **(c)** corresponding to Sample #6 represents a blurred yellow colored domains inside the strut of the lattice. This image elucidates the creation of PI aerogel in the cracked openings in polyacrylate resins caused by exposure to DMF and penetration by the precursors of PI. The fibrillar solid network structures of the PI aerogel materials was seen formed at the shell of the sample as presented in the inset of Fig. 4 **(d)**. The thickness of the yellow boundary in the optical images (Fig. 4b and c) is shown to be approximately 50 μm. However, a precise measurement of the boundary thickness from the SEM micrograph (Fig. 4d) confirmed uniform thin layers of PI coating with thickness below approximately 10 μm. In **Figure S4 (a)**, the edge surface of Sample #2 specimen is of sharp wedge-shape caused by the inherent resolution of layer-by-layer SLA printing used. After the PI coating, the surface morphology became significantly smoother than the uncoated sample as shown in **Figure S4 (b).**

We next investigated the mechanical properties of these tetrakaidekahedral lattices as shown in Fig. 5 **(a)**. With the exception of Sample #1 specimen, most of the lattices exhibited similar strain at break as

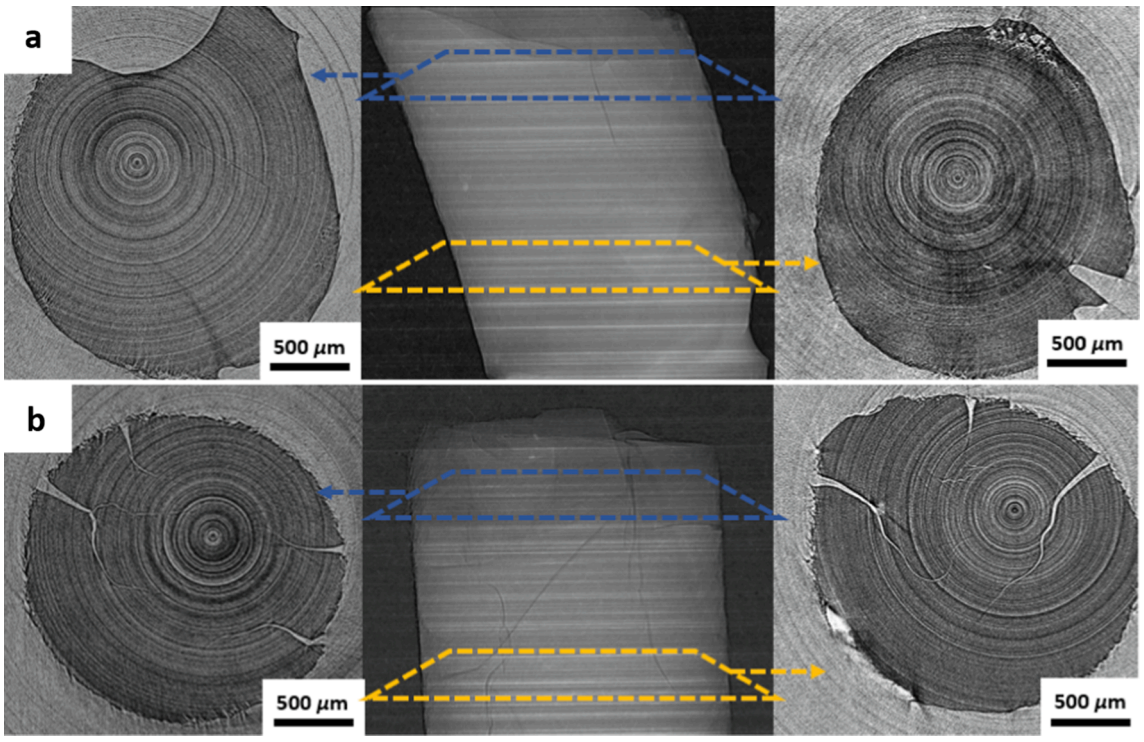

Fig. 6. X-ray μCT images of (a) #5 cured PI-coated lattice with (center) side-view and (left and right) cross-section at top and bottom plane and (b) #6 expanded PI-coated lattice (center) side-view and (left and right) cross-section at top and bottom plane. The radial shapes in the images are due to the background from the sample stage.

presented in Fig. 5**(d)**. We can elucidate that the tetrakaidekahedral lattice can maintain its global structure intact if the polymer network has low crosslink density. The compressive modulus in Fig. 5 **(b)** was calculated from the slope of the initial linear portion of stress vs strain curve of Fig. 5 **(c)**. All post-cured Samples-#2, #4 and #5-showed notably higher modulus than uncured samples. The solvent-aged Sample #3, #6, and #7 tend to have lower modulus than those not subjected to solvent aging attributed to the cracks in the struct structures. Unlike the post-curing or the solvent-aging, the coating did not significantly affect the mechanical property of the lattices.

To further correlate the mechanical performance and damages induced by solvent exposure, we investigated the effect of post-curing process and aging in solvent with the corresponding defects in the samples by using the X-ray μCT. In Fig. 6 **(a),** corresponding to Sample #5 (cured and PI-coated), the wedge-like cracks are observed near the surfaces, but no major cracks were observed near the core. In contrast, many branch-like cracks were observed in the case of Sample #6 (solvent aged, PI-coated) as in Fig. 6 **(b)**. These fractures in the expanded samples could have occurred by crack formation induced by the penetration of the solvent molecules in less crosslinked regions. In contrast, the abundant crosslinked networks inhibited the crack propagation from the edge, and only local crack appeared near the edge in Fig. 6 **(a)**. Similar behavior can be observed in **Figure S5 (a)** and **Figure S5 (b)**, where solid deposition is seen in the case of expanded samples due to crack formation.

Up to this point, the paper focused on establishing an innovative manufacturing technique to obtain polyimide aerogel coated tetrakaidecahedron lattices and to study the effect of various post-processing conditions on the morphology and mechanical strength of the resultant structures. Subsequently, we delved into several potential

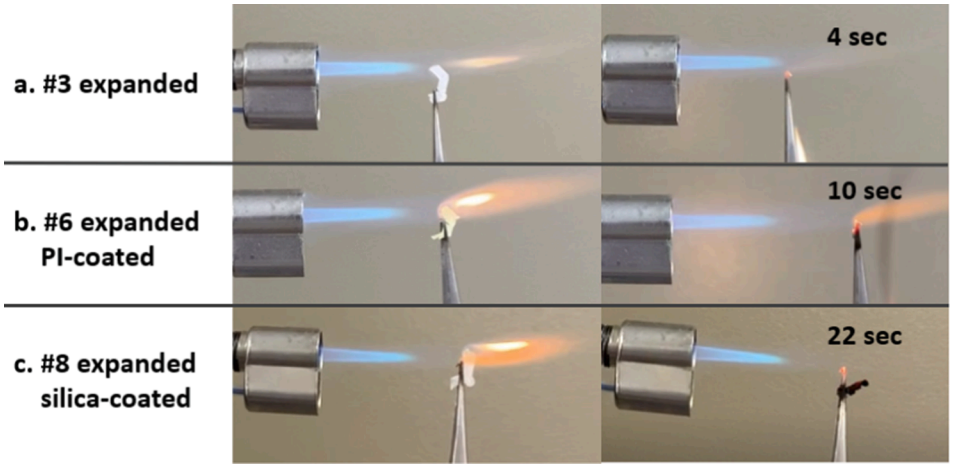

Fig. 7. Flame test of (a) #3 expanded, (b) #6 expanded_PI coated and (c) #8 expanded_silica-coated struts from tetrakaidekahedral lattices.

applications for these structures using polyimide, silica, and Kevlar aerogels as coatings. First, we investigated the flame retardant property of the fragment of the lattices by combustion test because aerogels are promising materials for insulation applications. The interconnected-network morphology of the aerogels along with very low thermal conductivity make aerogels resistant to fire. The polyacrylate resin is not a flame-retardant material, therefore, it was entirely decomposed in 4 s. Thus, adding an aerogel layer can help make the 3D-printed structures more resistant to fire. As we expected, aerogel coating influenced the retardation of the decomposition of the samples. Although the polyimide aerogel coating was rapidly decomposed at 550 °C according to TGA data in Fig. 3**(a)** and a relatively thin PI coating was formed on the surface of the lattice, it delayed the combustion of the polyacrylate for 6 s.

To further investigate the capabilities of aerogel in enhancing the fire retardance performance of the SLA printed structures, we prepared one more lattice specimen, Sample #8, coated by silica aerogel, which is a well-known flame-resistant material. [33,36,37] **Figure S6** indicates successful fabrication of silica aerogel coatings on the lattice. The results of the flame test are summarized in Fig. 7. From the flame test, it can be observed that the silica aerogel coating played a significant role in retarding the flame for additional 18 s compared to the acrylate resin. Even though the flame retardant performance of polyimide aerogel was not better than silica aerogel, this test is valuable in demonstrating that the thin polyimide aerogel coating presented an insulation function, thus protecting the internal materials.

Rendering the surface of the tetrakaidecahedron lattice porous by means of an aerogel coating bestows the resultant structures with additional advantages such as adsorption and filtration capabilities. Aerogels possess an interconnected network with a large number of mesopores leading to a large surface area. These properties are desired for nanoparticle filtration from air or water. We demonstrated the capability of the coated lattices in removal of methylene blue dye from water and NaCl nanoparticles from air. These results proved that the lattices can be modified to filter out the toxic cationic dyes from wastewater or to remove the nanoparticle impurities from air.

The organic pollutants in the form of dyes in both industrial and agricultural wastewaters pose a serious threat to the environment as well as human health. Methylene blue (MB) is one such commonly known organic dye which is used regularly in staining of cotton, wool, silk and during biological staining processes. [38] Although aerogels have high adsorption capabilities, they are not practical for dye adsorption applications because of their low mechanical strength. Thus, the coated lattices introduced in this study present a viable option for this purpose. To demonstrate that the coated lattices have the ability to remove organic dyes from water, an aqueous solution of methylene blue dye was used. The concentration of methylene blue dye solution was 0.01 g/L. A strut of lattice of length ~ 4 mm was immersed in 2 mL of the dye solution and allowed to reach an equilibrium in 5 days.

It was observed that sample #1 corresponding to the as-printed sample and sample #8 depicting the silica-aerogel coated sample showed the least change in the intensity of the blue color of the MB dye solution. The PI-coated lattices i.e., sample #6 and sample #7, displayed lower intensity of the color indicating that the concentration of MB in the solution had reduced because of the adsorption due to the PI aerogel layer. Finally, it was noted that sample #9 corresponding to the Kevlar aerogel coated lattice resulted in a clear solution and complete adsorption of MB dye from water. These results suggest that even a thin layer of aerogel on the lattice structure can impart adsorption properties to the SLA printed metamaterial structure which can be used for separation of nanometer sized impurities from water.

To quantify the above results, another strut of the coated lattices of length ~ 4 mm was immersed in 4 mL of the 0.01 g/L solution of MB. After 5 days, the concentration of the residual MB dye in water was determined with the help of an ultraviolet–visible (UV–vis) spectrophotometer. The results obtained are listed in Table 3. The values from

Table 3
Amount of dye adsorbed per unit weight (mg/g) for different lattice specimens.

Specimen	Specimen mass (g)	Dye adsorbed per unit weight (mg/g)
#1 as-printed	0.022	0.10
#8 expanded_silica-coated	0.011	0.32
#6 expanded_PI-coated	0.015	0.61
#7 expanded_cured_PI-coated	0.009	0.71
#9 expanded_Kevlar-coated	0.013	2.14

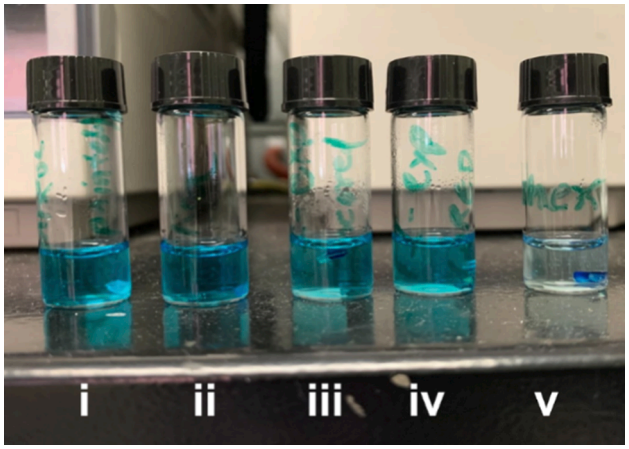

Fig. 8. Images of the dye solution after 5 days for (i) #1 as-printed, (ii) #8 expanded_silica-coated, (iii) #6 expanded_PI-coated, (iv) #7 expanded_cured_PI-coated, and (v) #9 expanded_Kevlar-coated.

Table 3 follow the trend observed in Fig. 8. It should be noted that MB is an aromatic cationic dye (**Figure S8**), and the adsorption of MB on a surface majorly occurs due to one or more of these three possible mechanisms- electrostatic attractions, hydrogen bonding with the nitrogen atoms, and the $\pi-\pi$ stacking interactions with the aromatic rings [38]. A higher adsorption capacity is seen from PI aerogel and Kevlar aerogel owing to the $\pi-\pi$ stacking interactions with the aromatic rings which was absent in silica aerogel. The lattice coated with Kevlar aerogel (sample #9) shows the highest adsorption of MB per unit weight because of the inherently high adsorption capabilities of the Kevlar aerogel. Because of the electrostatic nature and presence of amide hydrogens, Kevlar aerogel shows higher adsorption of the MB dye through electrostatic attractions. As seen from Table 3, it can be discerned that sample #9 showed capabilities to separate MB molecules from water which were almost 21 times higher than the as-printed samples which has negligible adsorption ability.

The effectiveness of the coated lattices for filtration of airborne nanoparticles was evaluated using sample #9 i.e., Kevlar coated tetrakaidecahedral lattice. For air filtration experiment, a TSI-8130 air filter tester (TSI Inc. Shoreview, MN) was used. This tester generated sodium chloride (NaCl) nanoparticles with diameters in the range of 25 nm- 150 nm. Sample #9 was placed in the sample holder of the tester and the airborne NaCl nanoparticles at the air flow rate of 20 L/min were allowed to pass through the sample for 40 min. **Figure S9** shows the experimental setup for air filtration experiment. From the difference in the weight of the sample measured before and after passing of the nanoparticles, it was determined that 2.5 mg of nanoparticles were captured in the sample.

Scanning electron microscopy was performed to observe the microstructure of the aerogel layer and to determine the presence of any NaCl nanoparticle in the aerogel network. Four struts from arbitrary locations of the lattice were used for this purpose. As seen from Fig. 9, it is evident that the nanoparticles were trapped in the pores of the aerogel structure

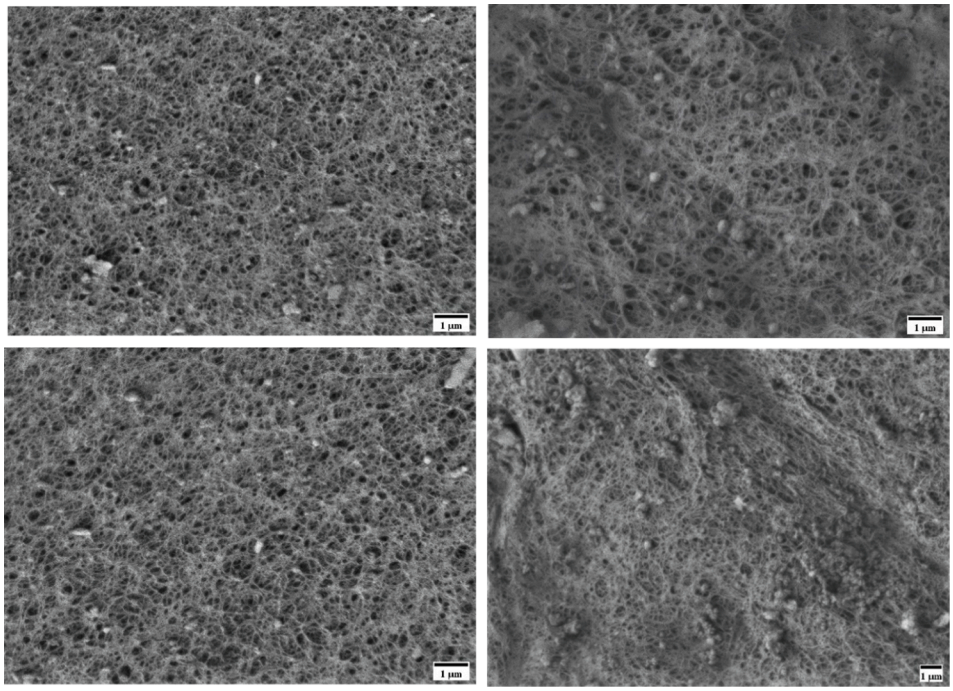

Fig. 9. SEM images of the surface of struts of sample #9 expanded_Kevlar-coated lattice collected from different parts of the sample after passing NaCl nanoparticles through the lattice at 20 L/min for 40 mins.

due to presence of the mesopores (2–50 nm). Similar observations were made in earlier studies [18–20,22]. The images taken from various parts of the sample and the presence of nanoparticles in all the images suggest that the entire surface was utilized in the filtration process. This test should be regarded as a proof of concept that the superficially porous metamaterials produced by the technique described in this paper will have the ability to filter out airborne nanoparticle impurities. For anyone interested to study the efficiency of such materials in greater detail, an experiment can be designed where the nanoparticles should be passed through the samples enclosed in a glass sample holder to prevent the passage of air through the sample cavities.

It should also be noted that the metamaterial design and the aerogel chemistry can be chosen as per the required application and the morphology of the aerogel layer can be manipulated through the post-processing steps. Taking this into account, it can be concluded that these superficially porous metamaterials mark the advent of one of a kind futuristic material which can benefit from the porous aerogel surface coatings along with the extraordinary properties of metamaterials.

4. Conclusion

This work introduced a facile method for coating functional aerogel layers onto 3D-printed metamaterials thus adding functionality to simple lattice type skeletal structures and deriving desired mechanical strength from the lattice structures to supplement the mechanically weak, but functionally rich aerogel layers. The aerogel coating layers of PI, silica, and Kevlar were all deposited onto acrylate struts and their utility in flame retardance and in airborne nanoparticle filtration established. The work also presented a step by step process for materials selection based on surface energy considerations and cleverly used swelling phenomena by the solvents for infusion of the acrylate material struts with corresponding sol of silica, PI, and Kevlar. There are a large number of materials and structures that one can envision for producing metamaterial structures similar to the current work. Thus, this study provides a new approach to explore these combinations to potentially advance 3D materials fabrication for membrane and other thermally stable metamaterial architectures.

CRediT authorship contribution statement

Piljae Joo: Conceptualization, Methodology, Writing – original draft. **Aparna Agrawal:** Data curation, Methodology, Writing – original draft. **Yimin Yao:** Investigation. **Nicholas Teo:** Investigation. **Sadhan C. Jana:** Supervision, Writing – review & editing.

Declaration of Competing Interest

The authors declare that they have no known competing financial interests or personal relationships that could have appeared to influence the work reported in this paper.

Data availability

Data will be made available on request.

Acknowledgement

This work was partially supported by ACS Petroleum Research Fund under grant number PRF# 59000-ND7 and by U.S. National Science Foundation under grant number CMMI 1826030.

Data availability

The raw/processed data required to reproduce these findings cannot be shared at this time as the data also forms part of an ongoing study.

Appendix A. Supplementary material

Supplementary data to this article can be found online at https://doi.org/10.1016/j.eurpolymj.2022.111575.

References

[1] S.C.L. Fischer, L. Hillen, C. Eberl, Mechanical Metamaterials on The Way from Laboratory Scale to Industrial Applications: Challenges for Characterization and Scalability, Materials 13 (16) (2020) 1–16, https://doi.org/10.3390/MA13163605.

[2] R.A. Shelby, D.R. Smith, S. Schultz, Experimental Verification of a Negative Index of Refraction, Science 292 (5514) (2001) 77–79, https://doi.org/10.1126/science.1058847.

[3] J.U. Surjadi, L. Gao, H. Du, X. Li, X. Xiong, N.X. Fang, Y. Lu, Mechanical Metamaterials and Their Engineering Applications, Adv. Eng. Mater. 21 (3) (2019) 1–37, https://doi.org/10.1002/adem.201800864.

[4] H.T. Chen, W.J. Padilla, J.M.O. Zide, A.C. Gossard, A.J. Taylor, R.D. Averitt, Active Terahertz Metamaterial Devices, Nature 444 (7119) (2006) 597–600, https://doi.org/10.1038/nature05343.

[5] V.M. Shalaev, W. Cai, U. Chettiar, H.K. Yuan, A.K. Sarychev, V.P. Drachev, A. V. Kildishev, Negative Index of Refraction in Optical Metamaterials, Optics InfoBase Conference Papers 30 (24) (2005) 3356–3358, https://doi.org/10.1364/fio.2005.ftuc2.

[6] C. Enkrich, F. Pérez-Willard, D. Gerthsen, J.F. Zhou, T. Koschny, C.M. Soukoulis, M. Wegener, S. Linden, Focused-Ion-Beam Nanofabrication of near-Infrared Magnetic Metamaterials, Adv. Mater. 17 (21) (2005) 2547–2549, https://doi.org/10.1002/adma.200500804.

[7] D. Chanda, K. Shigeta, S. Gupta, T. Cain, A. Carlson, A. Mihi, A.J. Baca, G. R. Bogart, P. Braun, J.A. Rogers, Large-Area Flexible 3D Optical Negative Index Metamaterial Formed By Nanotransfer Printing, Nat. Nanotechnol. 6 (2011) 402–1207, https://doi.org/10.1038/NNANO.2011.82.

[8] K.E. Evans, A. Alderson, Auxetic Materials: Functional Materials and Structures from Lateral Thinking!, Adv. Mater. 12 (9) (2000) 617–628.

[9] K.K. Saxena, R. Das, E.P. Calius, Three Decades of Auxetics Research – Materials with Negative Poisson's Ratio: A Review, Adv. Eng. Mater. 18 (11) (2016) 1847–1870, https://doi.org/10.1002/adem.201600053.

[10] S. Hengsbach, A.D. Lantada, Direct Laser Writing of Auxetic Structures: Present Capabilities and Challenges, Smart Mater. Struct. 23 (8) (2014) 085033, https://doi.org/10.1088/0964-1726/23/8/085033.

[11] L.L. Hu, T.X. Yu, Dynamic Crushing Strength of Hexagonal Honeycombs, Int. J. Impact Eng. 37 (5) (2010) 467–474, https://doi.org/10.1016/j.ijimpeng.2009.12.001.

[12] D.J. McGregor, S. Tawfick, W.P. King, Mechanical Properties of Hexagonal Lattice Structures Fabricated Using Continuous Liquid Interface Production Additive Manufacturing, Addit. Manuf. 2019 (25) (October 2018) 10–18, https://doi.org/10.1016/j.addma.2018.11.002.

[13] T.A. Schaedler, A.J. Jacobsen, A. Torrents, A.E. Sorensen, J. Lian, J.R. Greer, L. Valdevit, W.B. Carter, Ultralight Metallic Microlattices, Science 334 (6058) (2011) 962–965, https://doi.org/10.1126/science.1211649.

[14] L. Gao, J. Song, Z. Jiao, W. Liao, J. Luan, J.U. Surjadi, J. Li, H. Zhang, D. Sun, C. T. Liu, Y. Lu, High-Entropy Alloy (HEA)-Coated Nanolattice Structures and Their Mechanical Properties, Adv. Eng. Mater. 20 (1) (2018) 1–8, https://doi.org/10.1002/adem.201700625.

[15] M.A.B. Meador, E.J. Malow, R. Silva, S. Wright, D. Quade, S.L. Vivod, H. Guo, J. Guo, M. Cakmak, Mechanically Strong, Flexible Polyimide Aerogels Cross-Linked with Aromatic Triamine, ACS Appl. Mater. Interfaces 4 (2) (2012) 536–544, https://doi.org/10.1021/am2014635.

[16] Q. Zheng, L. Fang, H. Guo, K. Yang, Z. Cai, M.A.B. Meador, S. Gong, Highly Porous Polymer Aerogel Film-Based Triboelectric Nanogenerators, Adv. Funct. Mater. 28 (13) (2018) 1–9, https://doi.org/10.1002/adfm.201706365.

[17] C.A. García-González, M. Jin, J. Gerth, C. Alvarez-Lorenzo, I. Smirnova, Polysaccharide-Based Aerogel Microspheres for Oral Drug Delivery, Carbohydr. Polym. 117 (2015) 797–806, https://doi.org/10.1016/j.carbpol.2014.10.045.

[18] S.J. Kim, G. Chase, S.C. Jana, Polymer Aerogels for Efficient Removal of Airborne Nanoparticles, Sep. Purif. Technol. 156 (2015) 803–808, https://doi.org/10.1016/j.seppur.2015.11.005.

[19] S.J. Kim, P. Raut, S.C. Jana, G. Chase, Electrostatically Active Polymer Hybrid Aerogels for Airborne Nanoparticle Filtration, ACS Appl. Mater. Interfaces 9 (7) (2017) 6401–6410, https://doi.org/10.1021/acsami.6b14784.

[20] S.J. Kim, G. Chase, S.C. Jana, The Role of Mesopores in Achieving High Efficiency Airborne Nanoparticle Filtration Using Aerogel Monoliths, Sep. Purif. Technol. 166 (2016) 48–54, https://doi.org/10.1016/j.seppur.2016.04.017.

[21] Y. Wang, T. He, M. Liu, J. Ji, Y.u. Dai, Y. Liu, L. Luo, X. Liu, J. Qin, Fast and Efficient Oil-Water Separation under Harsh Conditions of the Flexible Polyimide Aerogel Containing Benzimidazole Structure, Colloids Surf., A 581 (2019) 123809, https://doi.org/10.1016/j.colsurfa.2019.123809.

[22] C. Zhai, S.C. Jana, Tuning Porous Networks in Polyimide Aerogels for Airborne Nanoparticle Filtration, ACS Appl. Mater. Interfaces 9 (35) (2017) 30074–30082, https://doi.org/10.1021/acsami.7b09345.

[23] S.G. Mosanenzadeh, Z. Saadatnia, S. Karamikamkar, C.B. Park, H.E. Naguib, Polyimide Aerogels with Novel Bimodal Micro and Nano Porous Structure Assembly for Airborne Nano Filtering Applications, RSC Adv. 10 (39) (2020) 22909–22920, https://doi.org/10.1039/d0ra03907a.

[24] N. Teo, P. Joo, E.J. Amis, S.C. Jana, Development of Intricate Aerogel Articles Using Fused Filament Fabrication, ACS Appl. Polym. Mater. 1 (7) (2019) 1749–1756, https://doi.org/10.1021/acsapm.9b00301.

[25] A. Agrawal, P. Joo, N. Teo, S.C. Jana, Fabrication and Characterization of Re-Entrant Honeycomb Polyurethane Aerogels, ACS Appl. Polym. Mater. 4 (5) (2022) 3791–3801, https://doi.org/10.1021/acsapm.2c00269.

[26] P. Joo, Y. Yao, N. Teo, S.C. Jana, Modular Aerogel Brick Fabrication via 3D-Printed Molds, Addit. Manuf. 46 (April) (2021), 102059, https://doi.org/10.1016/j.addma.2021.102059.

[27] C. Sun, N. Fang, D.M. Wu, X. Zhang, Projection Micro-Stereolithography Using Digital Micro-Mirror Dynamic Mask, Sens. Actuators, A 121 (1) (2005) 113–120, https://doi.org/10.1016/j.sna.2004.12.011.

[28] T.D. Ngo, A. Kashani, G. Imbalzano, K.T.Q. Nguyen, D. Hui, Additive Manufacturing (3D Printing): A Review of Materials, Methods, Applications and Challenges, Compos. B Eng. 143 (February) (2018) 172–196, https://doi.org/10.1016/j.compositesb.2018.02.012.

[29] I. Muha, A. Naegel, S. Stichel, A. Grillo, M. Heisig, G. Wittum, Effective Diffusivity in Membranes with Tetrakaidekahedral Cells and Implications for the Permeability of Human Stratum Corneum, J. Membr. Sci. 368 (1–2) (2011) 18–25, https://doi.org/10.1016/j.memsci.2010.10.020.

[30] W. Sir Thomson, On The Division of Space with Minimum Partitional Area, The London, Edinburgh, and Dublin Philosophical Magazine and Journal of Science 24 (151) (1887) 503, https://doi.org/10.1080/14786448708628135.

[31] N. Teo, S.C. Jana, Solvent Effects on Tuning Pore Structures in Polyimide Aerogels, Langmuir 34 (29) (2018) 8581–8590, https://doi.org/10.1021/acs.langmuir.8b01513.

[32] S. Gu, C. Zhai, S.C. Jana, Aerogel Microparticles from Oil-in-Oil Emulsion Systems, Langmuir 32 (22) (2016) 5637–5645, https://doi.org/10.1021/acs.langmuir.6b01043.

[33] Z.-L. Yu, N. Yang, V. Apostolopoulou-Kalkavoura, B. Qin, Z.-Y. Ma, W.-Y. Xing, C. Qiao, L. Bergström, M. Antonietti, S.-H. Yu, Fire-Retardant and Thermally Insulating Phenolic-Silica Aerogels, Angew. Chem. 57 (2018) 4538–4542.

[34] S. Wu, Calculation of Interfacial Tension in Polymer Systems, Journal of Polymer Science Part C: Polymer Symposia 34 (1) (1971) 19–30, https://doi.org/10.1002/polc.5070340105.

[35] J. Feng, X. Wang, Y. Jiang, D. Du, J. Feng, Study on Thermal Conductivities of Aromatic Polyimide Aerogels, ACS Appl. Mater. Interfaces 8 (20) (2016) 12992–12996, https://doi.org/10.1021/acsami.6b02183.

[36] T. Kashiwagi, J.W. Gilman, K.M. Butler, R.H. Harris, J.R. Shields, A. Asano, Flame Retardant Mechanism of Silica Gel/Silica, Fire Mater. 24 (6) (2000) 277–289.

[37] X. Zhang, X. Ni, C. Li, B. You, G. Sun, Co-Gel Strategy for Preparing Hierarchically Porous Silica/Polyimide Nanocomposite Aerogel with Thermal Insulation and Flame Retardancy, J. Mater. Chem. A 8 (19) (2020) 9701–9712, https://doi.org/10.1039/c9ta13011j.

[38] A.H. Jawad, R. Razuan, J.N. Appaturi, L.D. Wilson, Adsorption and Mechanism Study for Methylene Blue Dye Removal with Carbonized Watermelon (Citrullus Lanatus)Rind Prepared via One-Step Liquid Phase H_2SO_4 Activation, Surf. Interfaces 2019 (16) (November 2018) 76–84, https://doi.org/10.1016/j.surfin.2019.04.012.